

An empirical study on optic disc segmentation using an active contour model



M. Caroline Viola Stella Mary^{a,b}, Elijah Blessing Rajsingh^b, J. Kishore Kumar Jacob^c,
D. Anandhi^c, Umberto Amato^d, S. Easter Selvan^{e,*}

^a Department of Information Technology, Francis Xavier Engineering College, Tirunelveli 627003, Tamil Nadu, India

^b School of Computer Science and Technology, Karunya University, Coimbatore 641114, Tamil Nadu, India

^c Department of Ophthalmology, Tirunelveli Medical College Hospital, Tirunelveli 627011, Tamil Nadu, India

^d Istituto per le Applicazioni del Calcolo 'Mauro Picone'—Sede di Napoli, Consiglio Nazionale delle Ricerche, Via Pietro Castellino 111, Napoli 80131, Italy

^e GIPSA-Lab, CNRS UMR5216, Grenoble Campus, St. Martin D'Hères F-38402, France

ARTICLE INFO

Article history:

Received 16 August 2014

Received in revised form 3 November 2014

Accepted 6 November 2014

Available online 29 December 2014

Keywords:

Active contour models

Circular Hough transform

Glaucoma

Optic disc segmentation

ABSTRACT

The accurate segmentation of the optic disc (OD) offers an important cue to extract other retinal features in an automated diagnostic system, which in turn will assist ophthalmologists to track many retinopathy conditions such as *glaucoma*. Research contributions regarding the OD segmentation is on the rise, since the design of a robust automated system would help prevent blindness, for instance, by diagnosing glaucoma at an early stage and a condition known as *ocular hypertension*. Among the evaluated OD segmentation schemes, the active contour models (ACMs) have often been preferred by researchers, because ACMs are endowed with several attractive properties. To this end, we designed an OD segmentation scheme to infer how the performance of the well-known *gradient vector flow* (GVF) model compares with nine popular/recent ACM algorithms by supplying them with the initial OD contour derived from the *circular Hough transform*. The findings would hopefully equip a diagnostic system designer with an empirical support to ratify the choice of a specific model as we are bereft of such a comparative study. A dataset comprising 169 diverse retinal images was tested, and the segmentation results were assessed by a gold standard derived from the annotations of five domain experts. The segmented ODs from the GVF-based ACM coincide to a greater degree with those of the experts in 94% of the cases as predicted by the least overall *Hausdorff distance* value (33.49 ± 18.21). Additionally, the decrease in the segmentation error due to the suggested ACM has been confirmed to be statistically significant in view of the *p* values ($\leq 1.49 \times 10^{-9}$) from the *Wilcoxon signed-rank test*. The mean computational time taken by the investigated approaches has also been reported.

© 2014 Elsevier Ltd. All rights reserved.

1. Introduction

Detection of retinal anatomical features is crucial to clinically assess the health of the retina. To facilitate this task, automated diagnostic systems critically rely on an accurate optic disc (OD) detection procedure, in the sense that other anatomical features such as retinal blood vessels, macula, optic cup, and lesions can in turn be detected with reference to the OD location [1]. In particular,

the OD detection is extremely useful in diagnosing a retinopathy condition called *glaucoma*, which is the leading cause of blindness next to *cataract* [2]. According to Nayak et al. [3], glaucoma affects one in two hundred individuals around the age of 50, and one in ten above 80 years. Moreover, the detrimental effects of glaucoma surface only at a later stage, and hence it is commonly known as the “sneak thief of sight”. Interestingly though, the detection of this disease at an early stage will help to retard its progression thanks to medical advancements [4]. In other words, the structural change in the OD provides vital clues concerning the prognosis of glaucoma. Fueled by the diagnostic and prognostic significance, automatic OD detection schemes have been attempted by many and their design still remains as a vibrant research area [5].

An accurate OD segmentation with computer-aided techniques faces several challenges due to factors that are common to other

* Corresponding author. Tel.: +33 (0)619994720.

E-mail addresses: carolsam67@gmail.com (M.C.V.S. Mary), elijahblessing@karunya.edu (E.B. Rajsingh), abc12304@rediffmail.com (J.K.K. Jacob), dranandhij@gmail.com (D. Anandhi), u.amato@iac.cnr.it (U. Amato), easter-selvan.suvisheshamuthu@gipsa-lab.grenoble-inp.fr (S.E. Selvan).

medical images, for instance, boundary insufficiencies—missing edges and/or inadequate texture contrast between regions of interest (ROIs) and the background. On the other hand, manually segmenting the OD is not deemed admissible, since it is subject to impediments such as limited perception of the human eye, fatigue, and the availability of voluminous fundus image data. Therefore, developing algorithms that can reliably detect accurate OD boundaries with less computational overheads is an imperative research goal.

To provide an overview of the research efforts along this direction, a brief survey on the state-of-the-art OD segmentation schemes is in order. Lalonde et al. [6] reported a technique for the OD localization in color fundus images by combining a Hausdorff-distance-based template matching on edge maps and a pyramidal decomposition. Li and Chutatape [7] applied the principal component analysis on a color retinal photography to locate the OD and an active shape model to segment the same. Foracchia et al. [8] described the common directional pattern of retinal vessels with a geometrical parametric model, and identified the coordinates of the OD center with a simulated annealing technique. Niemeijer et al. [9] formulated the OD detection task as an optimization problem that fits a single point distribution model to a color fundus photograph. Youssif et al. [10] adopted a filter to match the expected directional pattern of retinal blood vessels in the vicinity of the OD, and segmented the vessels with a 2-D Gaussian matched filter to estimate the OD center. Lu and Lim [11] designed a line operator, which evaluates the intensity variation along multiple line segments with specific orientations and traversing through retinal image pixels. Lu [12] employed a circular transformation, wherein every retinal image pixel corresponding to the maximum image variation along multiple evenly-oriented radial line segments of fixed length constitutes the OD boundary.

In view of the inherent advantages of active contour models (ACMs), there is an emerging trend to make use of ACMs in OD segmentation tasks. In general, ACMs have been proven successful in image segmentation applications [13,14]. They are based on profound mathematical properties and efficient level-set-based numerical schemes. It is possible to achieve a sub-pixel accuracy of object boundaries with the ACMs [15]. They lend themselves to incorporate a prior knowledge, e.g., shape and intensity distribution [16]. Furthermore, they can be implemented to exploit several properties, e.g., edges, statistics, and texture, which are normally considered by other segmentation procedures. Besides producing quite regular contours, the segmented regions possess continuous boundaries. In addition, the level set theory offers a lot of flexibility in their implementation.

In that vein, a few interesting contributions involving an ACM to segment the OD are listed below. Lowell et al. [17] presented an algorithm, which localizes the OD using a specialized template matching, and then segments it with a deformable contour model. Unlike other edge detection methods, this model reliably segmented the ODs from images of diseased retinæ including strong distractors. Chr stek et al. [18] presented an automated algorithm for the OD segmentation in scanning-laser-tomography images. This method is based on morphological operations, the Hough transform, and an anchored ACM derived from the works of Cohen and Cohen [19] and Kucera [20]. Xu et al. tackled the problem of vessel occlusion that interferes with the OD segmentation in [21] by incorporating a knowledge-based clustering of contour points and a smoothing update into the original *snake* by Kass et al. [22]. Joshi et al. [24] enhanced the robustness of the ACM by Chan and Vese [23] against variations in the vicinity of the OD region by integrating the local image information around each point of interest in a multidimensional feature space; the segmentation results were shown to be consistent with respect to geometric and photometric variations in retinal images. Yu et al. developed

a fast and fully automatic OD segmentation algorithm in [25], which applies an initial OD contour identified with the template matching to a hybrid level set model proposed by Zhang et al. [26]. The robustness and accuracy of segmented OD boundaries are attributed to the fact that the model in [25] combines the region and local gradient information in the retinal images.

Notwithstanding a dedicated research effort in the design of ACM-based image segmentation tools, as far as we know, a rigorous comparison of a wide range of ACM techniques has not yet been reported in the context of the OD segmentation. In fact, empirical results from an exhaustive study involving popular ACM methods on a large collection of retinal images would be suggestive of the kind of ACM scheme to be advocated in the design of a fully automated OD segmentation system for clinical screening purposes. Within this framework, we methodically compared the OD segmentation results from ten theoretically well-established ACM techniques supplied with 169 diverse retinal fundus images annotated by domain experts. To be fair in our comparison, the ACM algorithms were initialized with a contour obtained by a morphological process and the *circular Hough transform* (CHT). Unless the resultant contour warrants further tuning, the default parameters were kept unaltered for the ACM models.

2. Materials and methods

2.1. Test database

The open retinal image database for optic nerve evaluation (RIM-ONE) is an online dataset of 169 retinal fundus images annotated by five experts in ophthalmology [27]. The retinal photograph is captured (with non-mydratic fundus camera) while the pupil is not dilated with flash intensities that avoid saturation. The images are stored in the red-green-blue (RGB) color bitmap (i.e., BMP) format with intensities ranging from 0 to 255 in each channel. The domain experts have classified the images in the dataset into the following categories: 118 normal eye (non-glaucomatous), 12 early glaucoma, 14 moderate glaucoma, 14 deep glaucoma, and 11 *ocular hypertension* (OHT). A gold standard has been provided for each image from the contours demarcated by five experts.

2.2. Overview of the proposed approach

A schematic diagram of the proposed methodology to enhance the segmentation accuracy of the OD is presented in Fig. 1. The retinal images under investigation are preprocessed using the *adaptive histogram equalization* in the red channel, which facilitates an accurate OD identification due to the image contrast improvement. Subsequently, the morphological processing is performed using a line operator to remove any blood vessel present in the image. Following the preprocessing, the CHT is applied to estimate the contour that roughly encloses the circular-shaped OD. Based on the empirical study involving ten well-known ACM algorithms, which is deferred to Section 6, the *gradient vector flow* (GVF) model is recommended in our work. Note that the GVF model is acclaimed to be a fast and hybrid level set method, which fine-tunes the contour initialized with the CHT until it accurately fits the boundary of the OD.

3. Preprocessing

Retinal images usually contain noise due to interference of various phenomena. Nonuniform illumination is one such problem because of the complexity of the image acquisition system. The noise and artifacts thus introduced complicate the retinal image analysis. For instance, they may cause only minor differences

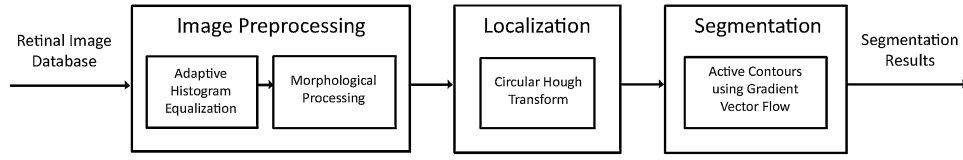


Fig. 1. Schematic diagram of the proposed OD segmentation method.

between normal and abnormal tissues. Precisely, noise affects the process of measuring parameters in retinal images. Hence preprocessing is an essential step in order to remove noise and artifacts present in these images. The adaptive histogram equalization is applied to compensate for the illumination artifacts [10]. As the name implies, the adaptive technique generates several histograms, each one corresponding to an image neighborhood for computing a transformation function, to modify the brightness levels of pixels belonging to that neighborhood. As a consequence, the contrast of an image is locally improved and the details are enhanced.

Blood vessels originate from the OD, and appear as deep red or orange red filaments of progressively diminishing width. As they interfere with the detection of the OD, blood vessels are to be removed beforehand. A common practice is to carry out a morphological preprocessing prior to locating the OD, since this step filters out the blood vessels and exudates present in the retinal image [28]. In principle, the *opening* operation tends to smooth an image contour, whereas the *closing* is meant to fuse narrow breaks and to generate vessel masks. While the opening suppresses bright details, closing annihilates dark ones, provided the details remain smaller than the structuring element. A rotating structuring element, which is 1° to 6° apart and having enough length to traverse vessels and erase them, is employed in our application. Fig. 2 depicts preprocessing of the red and green channels from the RGB fundus image. Since the blood vessels are more prominent in the green channel, the red one is used for further processing.

4. OD localization

In retinal image analysis, accurately locating the OD in the presence of exudates is crucial due to the following reason. The exudates as well as the OD appear as clusters of high intensity pixels, which would pose challenges to an intensity-based OD segmentation scheme. We rely on the CHT to distinguish between the exudates and OD, since the CHT is well-suited for localizing the circular- or elliptic-shaped OD region [29]. The CHT is applied to the binary image resulting from the morphological processing. The preprocessed gray-scale images are converted to binary images (see Fig. 2(e) and (i)) with the help of gray-scale thresholds, which are selected in an unsupervised manner as described in [30]. This threshold selection scheme utilizes only the zeroth- and the first-order cumulative moments of the gray-scale histogram, and thus remains simple. The black pixels of the binary image constitute the approximate boundary of the OD, whereas the white ones represent the background. The transform maps a point (x, y) corresponding to a black pixel in the binary image to a truncated conical surface whose upper and lower radii (r_{\max} and r_{\min} , respectively) are determined by the a-priori knowledge of the OD radius' range (refer to Fig. 3(a)). In other words, a point in the image space is mapped to a truncated conical surface in the parameter space. Fig. 3(a) illustrates the generation of three truncated cones corresponding to three points on the perimeter of the binary image. As the CHT traverses through all the black pixels in the binary image, a three dimensional *accumulation matrix* will store the number of intersections of the truncated conical surfaces. The position of a cell in the accumulation matrix denotes a “potential” center and the radius

of the OD, and the value stored in the cell implies how probable it is to be the “true” center and radius. Evidently, the triplet $(\hat{a}, \hat{b}, \hat{r})$ associated with the accumulation cell that stores the largest value returns the actual center (\hat{a}, \hat{b}) and the radius \hat{r} of the OD region. For instance, the application of CHT on the preprocessed binary image from the red channel in Fig. 2(e) gives rise to the *Hough circle* as displayed in Fig. 3(b). Subsequently, the ACM method is initialized with a contour derived from the Hough circle.

In our experiments, an estimate of the OD radius r_{guess} is considered to be either 150 or 260 pixel units depending on whether the retinal image resolution is less or more than 512×512 . The r_{\min} and r_{\max} values are selected as 80% and 120% of r_{guess} , respectively. Thus a reliable and accurate boundary of the OD is delineated with the Hough circle as demonstrated in Fig. 4(a), since the OD is the only large circular object inside the ROI. Nonetheless, the presence of *peripapillary atrophy* (PPA) at the OD boundary may interfere with the OD detection process, leading to its inaccurate localization as depicted in Fig. 4(b).

5. OD segmentation

Following the localization of the OD region, the segmentation scheme should accurately demarcate the boundary of the OD to help track the progression of eye diseases. Naive segmentation algorithms that do not take the edge smoothness and continuity properties into account may fall short of accurately detecting the OD boundary. On the contrary, an ACM otherwise known as the snake is a promising alternative, as it relies on the gradient as well as the spatial distribution at a specific point to verify the presence of an edge. Aside from this merit, as explained in what follows, the snake can be adapted to capture even concavities on the OD boundary. A comprehensive list of advantages in resorting to ACMs has already been included in Section 1.

The snake in general is an energy minimizing deformable spline that satisfies the *Euler equation*. In the sequel, the Euler equation can be viewed as a force balance equation, $F_{\text{int}} + F_{\text{ext}}^{(p)} = 0$, where the internal force F_{int} discourages the snake to stretch and bend, while the external potential force $F_{\text{ext}}^{(p)}$ pulls the snake toward an image edge. However, the traditional snake inherently suffers from the failure to progress into (image) boundary concavities, and possesses only a limited capture range. To overcome these drawbacks, Xu and Prince replaced $F_{\text{ext}}^{(p)}$ in the force balance equation with a static external force field $\mathbf{v}(x, y)$, namely, GVF field, on the premise of the *Helmholtz theorem* [14]. An attractive consequence is that while \mathbf{v} minimizes an *energy functional*,¹ the snake is endowed with a large capture range and the ability to move into boundary concavities. In the energy functional, if the gradient of an *edge map*² $|\nabla f|$ is small, the smoothing term corresponding to the sum of the squares of the partial derivatives of \mathbf{v} is predominant. As a result, the energy minimization yields a slowly varying field in homogeneous image regions. By contrast, for a large $|\nabla f|$, the energy is

¹ $E = \int \int \mu(u_x^2 + u_y^2 + v_x^2 + v_y^2) + |\nabla f|^2 |\mathbf{v} - \nabla f|^2 dx dy$, where $u_x, u_y, v_x,$ and v_y are the partial derivatives of the vector field $\mathbf{v}(x, y) = [u(x, y), v(x, y)]$ according to [14].

² The edge map is a function $f(x, y)$ derived from an image $I(x, y)$ such that it has larger values near a desired image feature.

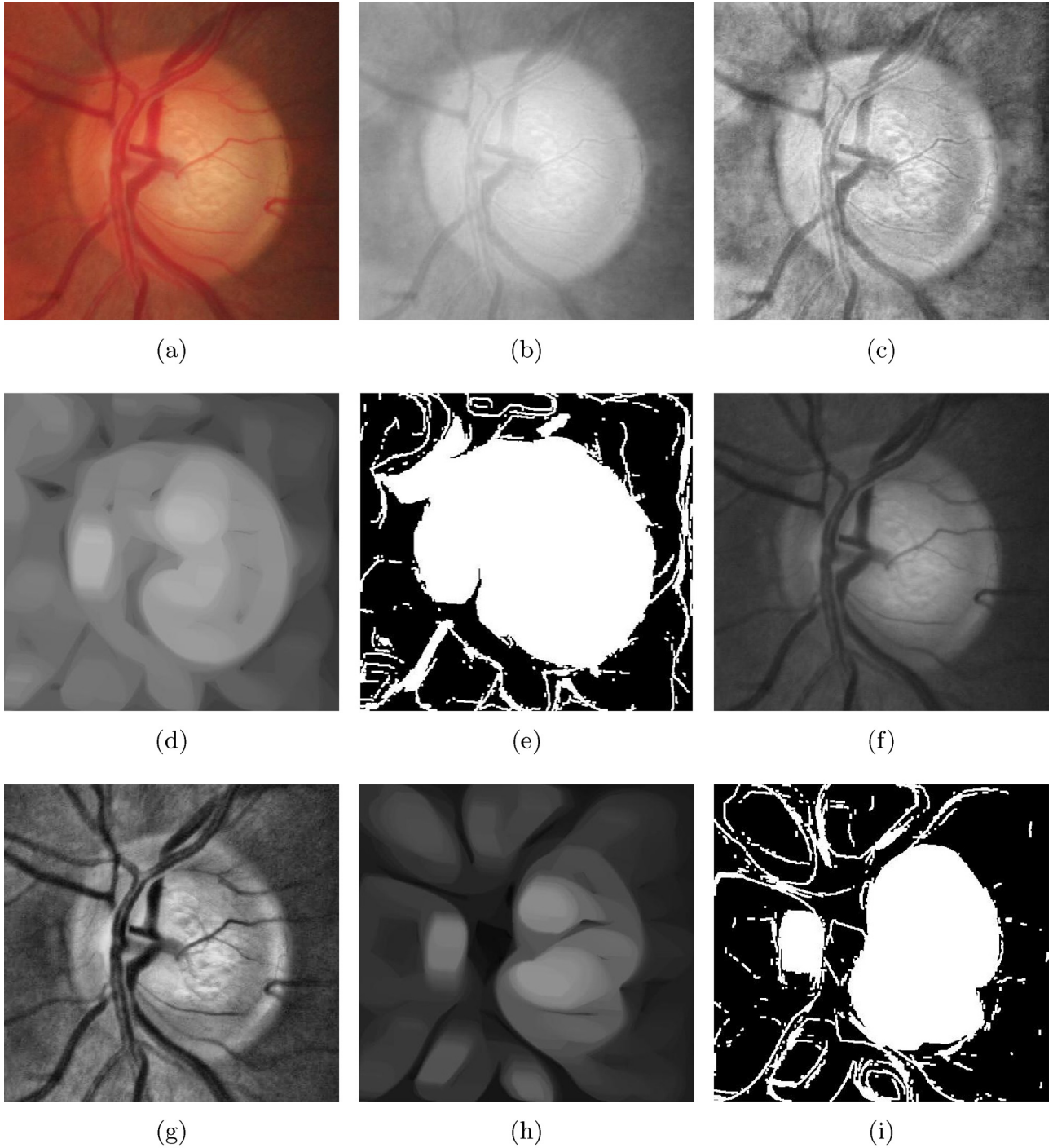


Fig. 2. Preprocessing results from the red and green channels of a retinal image. (a) Original image. (b) Red channel. (c) Adaptive histogram equalization of the red channel. (d) Morphological processing of the image in (c) using a line structuring element with 1° rotation. (e) Binary image of (d). (f) Green channel. (g) Adaptive histogram equalization of the green channel. (h) Morphological processing of the image in (g). (i) Binary image of (h).

minimized by bringing \mathbf{v} almost close to $|\nabla f|$, which is a desired effect. Furthermore, a regularization term μ in the energy functional maintains a good balance between both scenarios, and its choice remains directly proportional to the amount of noise.

In the present setting, the snake is initialized with the approximate OD boundary generated by the CHT. Subsequently, the minimization of the GVF-based energy functional forces the snake to undergo dynamic adaptation to the edges of the OD. The deformation of the snake iteratively proceeds until the energy functional reaches its minimum as illustrated in Fig. 5(a)–(d). Note that we

have empirically selected the value of μ to be 0.2, and observed an impressive segmentation accuracy with a faster rate of convergence.

6. Experimental results

We investigated the OD segmentation algorithm (hereafter referred to as Xu-ACM) described in Sections 3–5 with 169 retinal images from the RIM-ONE database mentioned in Section 2.1, which comprises the following fundus image categories:

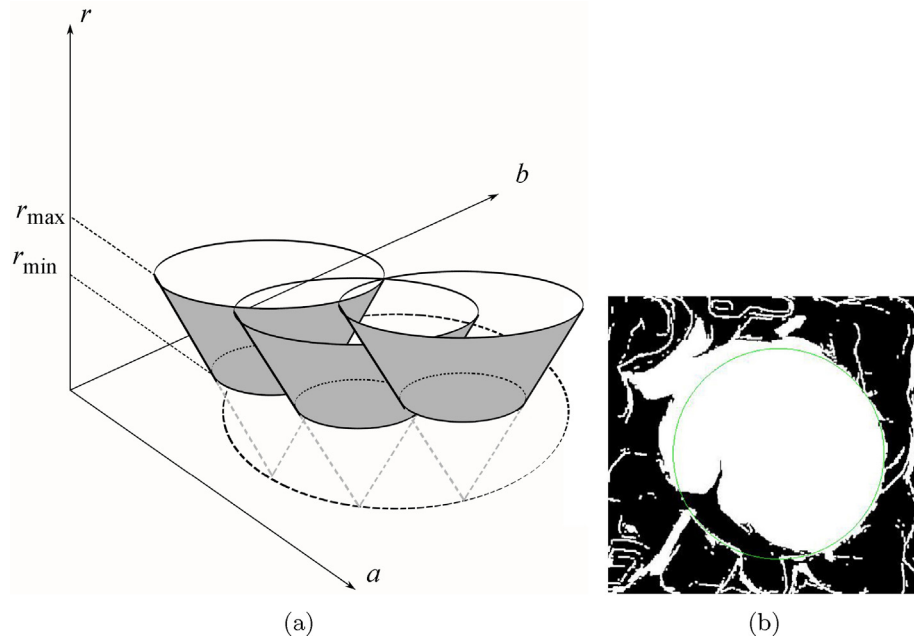


Fig. 3. (a) CHT maps three black pixels on the boundary of a binarized retinal image (dotted circle) to truncated cones (shaded in gray) in the parameter space. After applying the CHT to all the boundary pixels, the true center (\hat{a}, \hat{b}) and radius \hat{r} of the OD are deduced from the position of the accumulation cell $(\hat{a}, \hat{b}, \hat{r})$ containing the maximum number of intersections of the truncated cones. (b) The Hough circle shown in green is the result of applying the CHT on the preprocessed binary image from the red channel in Fig. 2(e). This in turn serves as the initial contour for the succeeding ACM method with slight alterations as described in Section 6.2. (For interpretation of the references to color in this figure legend, the reader is referred to the web version of this article.)

non-glaucomatous, early glaucoma, moderate glaucoma, deep glaucoma, and OHT condition. Aside from representative images with various degrees of glaucoma, the RIM-ONE database includes images under different lighting conditions and exposures.

6.1. Competing active contour models

To assess the merit of our approach, the segmentation results from the Xu-ACM (March 1998) have been quantitatively compared with an exhaustive list of the following popular or recently reported ACM techniques: (i) Caselles-ACM (June 1997) [13], (ii) Patrick-ACM (September 2000) [31], (iii) Chan-ACM (February 2001) [23], (iv) Shi-ACM (May 2008) [32], (v) Li2008-ACM (October 2008) [33], (vi) Lankton-ACM (November 2008) [34], (vii) Bernard-ACM (June

2009) [35], (viii) Li2010-ACM (December 2010) [36], and (ix) Wu-ACM (June 2013) [37].

- (i) **Caselles-ACM.** This approach is a geodesic formulation of active contours by introducing a term to the curve evolution models with the following consequences: improvement in the detection of boundaries, whose gradients differ significantly; and no requirement to estimate crucial parameters. Experimental study in [13] with various imagery demonstrates its capability to simultaneously detect several objects as well as both interior and exterior boundaries.
- (ii) **Patrick-ACM.** This scheme is a fast B-spline snake with a reduced number of parameters to optimize. Moreover, its formulation obviates the need for internal energies. It is reputed

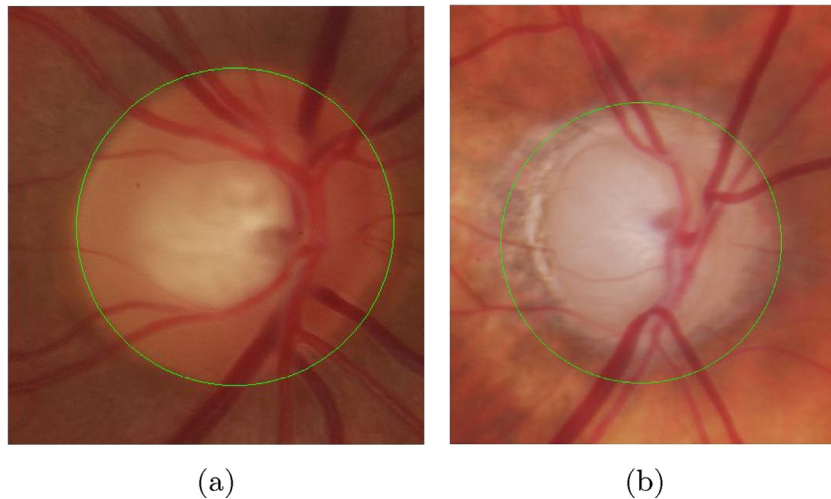


Fig. 4. OD localization is shown using green circles that encompass the OD: (a) accurately in the ROI from a normal retinal image; (b) incorrectly due to the presence of PPA at the OD boundary.

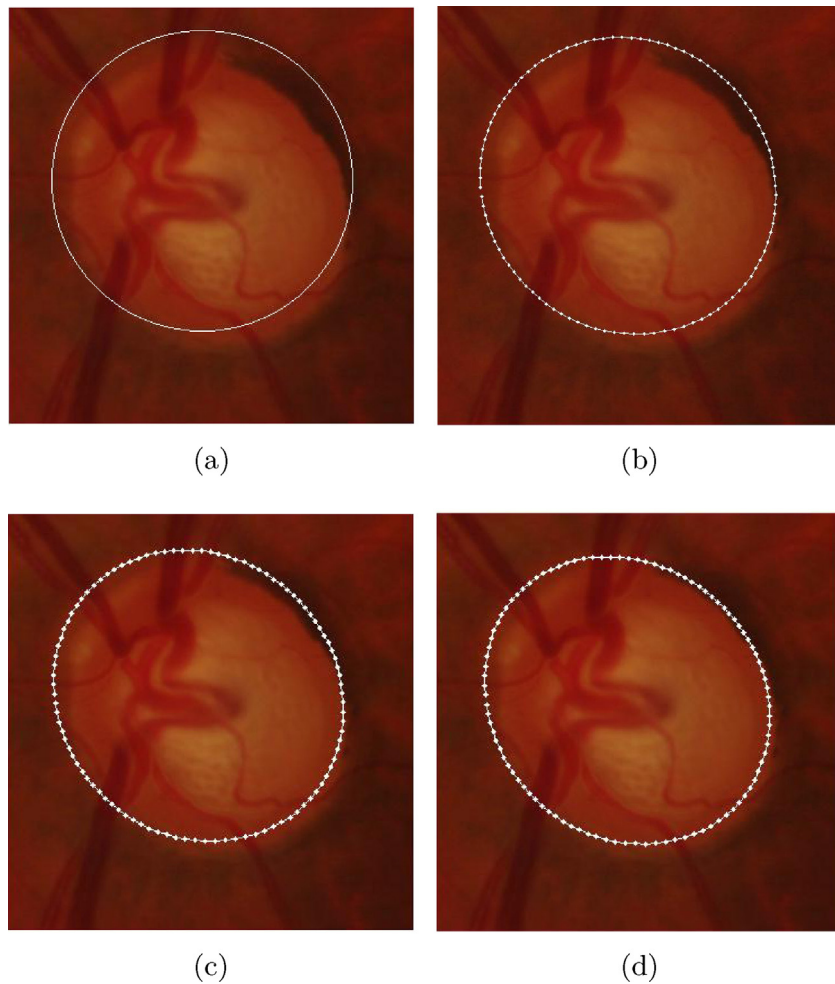


Fig. 5. The evolution of the snake to capture the OD boundary while minimizing the GVF-based energy functional. The adaptation of the snake to the contour of OD is displayed for the iteration 0, 100, 200, and 500 in (a)–(d).

to work well with poorly defined contours, e.g., biomedical images, and has been recommended to be initialized well.

- (iii) **Chan-ACM.** This region-based segmentation scheme is acclaimed to be a powerful and flexible method that can be applied to segment “difficult” images, i.e., detecting objects with boundaries not necessarily defined by the gradient or with very smooth boundaries. By contrast, this category of images would normally pose challenges to a classical thresholding or a gradient-based method. Furthermore, the Chan-ACM does not require the initial curve to surround the object of interest, and particularly when employed for the OD segmentation, it proceeds efficiently by first producing a first-order estimation of the PPA region.
- (iv) **Shi-ACM.** This level-set-based curve evolution has been developed to achieve a significant computational speedup by requiring only integer operations and refraining from solving partial differential equations (PDEs). Besides the method being suitable for real-time applications, it has been claimed in [32] that the performance of Shi-ACM remains on par with PDE-based implementations.
- (v) **Li2008-ACM.** It has been devised to cater to segmenting images with intensity inhomogeneities and weak object boundaries. This contour model exploits the intensity information in local regions at a controllable scale. The regularity of the level set function is intrinsically preserved by means of a regularization term, thereby ensuring an accurate computation and precluding an expensive initialization procedure.

- (vi) **Lankton-ACM.** It considers only local image statistics while evolving a contour, so that the framework befits well with segmenting objects having heterogeneous feature profiles. The benefits of localization amount to a robust and accurate segmentation of “challenging” images, where the approaches using global region-based energies tend to encounter a failure, as illustrated in [34]. The downside of this technique is its increased sensitivity to initialization with regard to global schemes.
- (vii) **Bernard-ACM.** The energy criterion is minimized in the Bernard-ACM with respect to the B-spline coefficients in contrast with other level-set-based ACM approaches. This formulation provides an overall control of the level set and avoids the reinitialization step of the level set. The advantages claimed for this approach in [35] are: simplified derivations of the cost function and an exact calculation of its gradient; and avoidance of arbitrary choices as the computations are exact. Due to the intrinsic smoothing of this approach, it efficiently deals with the additive noise during the segmentation tasks.
- (viii) **Li2010-ACM.** This model efficiently counteracts the irregularities faced by a conventional level-set-based ACM by introducing a distance regularization term, which maintains the desired shape of the level set function. As a consequence, the level set evolution is subject to a forward-and-backward diffusion effect, thereby intrinsically maintaining the regularity of the level set function in the course of its evolution. The Li2010-ACM has been claimed to offer a significant

computational advantage by allowing relatively large time steps, besides preserving the numerical accuracy in image segmentation implementations.

- (ix) **Wu-ACM.** A refinement of the GVF model has recently been proposed to rectify the susceptibility of the Xu-ACM model to weak edges as well as deep and narrow boundary concavities. An external force is incorporated into the model to adjust the diffusion process of the flow field adaptively in accordance with image characteristics. The salient advantage of Wu-ACM as claimed in [37] is that the active contours can be driven into deep and narrow concave regions of objects.

6.2. Implementation subtleties

The Matlab routines for the ACM algorithms were acquired from the following websites:

- Patrick-ACM: <http://www.mathworks.in/matlabcentral/fileexchange/28149-snake-active-contour>.
- Chan-ACM: <http://www.mathworks.in/matlabcentral/fileexchange/38358-active-geometric-shape-models>.
- Xu-ACM: <http://heim.ifi.uio.no/inf5300/data/GVF.m>.
- Caselles-ACM, Lankton-ACM, Shi-ACM, Li2008-ACM, and Bernard-ACM: <http://www.creatis.insa-lyon.fr/~bernard/creaseg/files/download.html>.
- Li2010-ACM: http://www.mathworks.in/matlabcentral/fileexchange/12711-level-set-for-image-segmentation/all_files.
- Wu-ACM: <http://www.mathworks.in/matlabcentral/fileexchange/42435-adaptive-diffusion-flow-active-contours-for-image-segmentation>.

The convergence criterion recommended in [38] is set for all the ACM methods that depends on the difference between the corresponding contour points pertinent to two consecutive iterations. If L^2 norm of the difference falls below a threshold value ϵ , meaning that there is no significant progress in the contour evolution, the algorithm is halted. The value of ϵ advocated in [38] is 0.0008, wherein a systematic comparative study of active contour snakes has been carried out.

The total iteration counts were set to be the same as the default values for the approaches other than the Patrick-ACM, Xu-ACM, Li2010-ACM, and Wu-ACM. In the Patrick-ACM and Xu-ACM, 200 iterations were allowed for the contour deformation, since the default value of 100 iterations is inadequate for the evolution of the contour in both the cases. Note, however, that the computational time taken by the Patrick-ACM and Xu-ACM is way less than the rest of the techniques. Similarly, it is required to have 100 iterations instead of a default value of 40 for the Li2010-ACM in view of the performance improvement. Whereas, the segmentation accuracy degrades significantly beyond ten iterations in the Wu-ACM, as indicated by a sharp increase in the average Hausdorff distance³ (HD) in Fig. 6, which compels us to fix the total number of iterations as ten. Notice that except in the case of Wu-ACM, whose performance deteriorates with an iteration count that exceeds the default value, the rest of the ACMs are executed for a surplus number of iterations as consolidated in Table 1 unless the halting criterion is not met.

The OD boundary detected by the CHT is used as such to initialize the contour for the Patrick-ACM, Chan-ACM, and Xu-ACM. However, for optimal OD segmentation results, the initial contour radii for the Caselles-ACM, Lankton-ACM, Shi-ACM, Li2008-ACM, Bernard-ACM, and Wu-ACM were determined by a rigorous

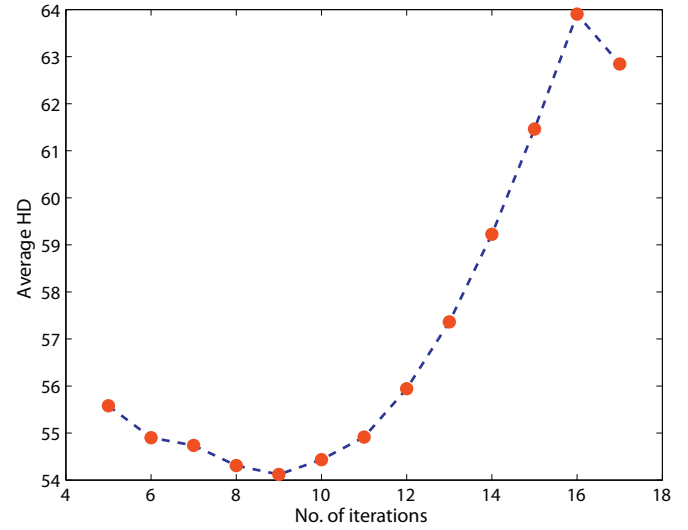


Fig. 6. Degradation of the OD segmentation performance in the Wu-ACM in terms of the increased average HD values as the iteration count exceeds ten.

empirical study to be 85%, 95%, 105%, 90%, 85%, and 85% of the resultant one from the CHT, respectively, as summarized in Table 1. Note that by construction, the Li2010-ACM will only admit a rectangular initial contour circumscribed by the boundary generated using the CHT.

6.3. Evaluation criterion

Definition 1 (Hausdorff distance [39]). Given two finite sets containing points $P = \{p_1, p_2, \dots, p_m\}$ and $Q = \{q_1, q_2, \dots, q_n\}$, the Hausdorff distance is defined as

$$H(P, Q) = \max(h(P, Q), h(Q, P))$$

where

$$h(P, Q) = \max_{p \in P} \min_{q \in Q} \|p - q\|$$

and $\|\cdot\|$ denotes the underlying norm on the points belonging to P and Q .

Intuitively, if $h(P, Q) = d$, then every point in P must lie within distance d from a point in Q . Therefore, $H(P, Q)$ measures the distance between the point in P that is the farthest from any point in Q and vice versa, thereby implying a “degree of mismatch” between the points in P and Q . Since we adopt this measure to compare a detected OD boundary with the one drawn by an expert, the sets P and Q contain the coordinates of the boundary pixels, and

Table 1

Summary of the iteration counts and the initial contour radii, which are set for various ACM methods applied to the OD segmentation task.

ACM method	Iteration count		Initial contour radius (% of CHT output)
	Default value	Set value	
Caselles-ACM	200	200	85
Xu-ACM	100	200	100
Patrick-ACM	100	200	100
Chan-ACM	100	100	100
Shi-ACM	200	200	105
Li2008-ACM	200	200	90
Lankton-ACM	200	200	95
Bernard-ACM	200	200	85
Li2010-ACM	40	100	Rectangle
Wu-ACM	120	10	85

³ The formal definition of Hausdorff distance is deferred to Section 6.3.

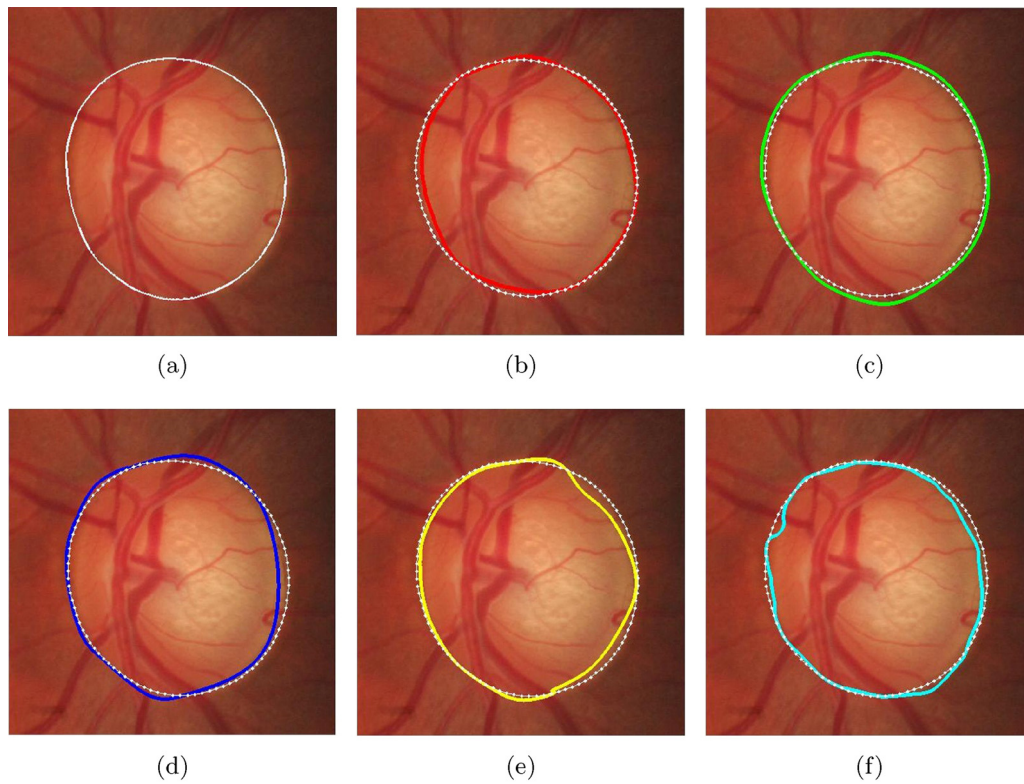


Fig. 7. (a) Detected OD boundary (white contour) using an ACM approach that is supplied with an initial contour from the CHT. (b)–(f) Delineation of the OD boundary (red, green, blue, yellow, and cyan contours) for the same retinal fundus image by five domain experts. (For interpretation of the references to color in this figure legend, the reader is referred to the web version of this article.)

$\|\cdot\|$ is considered as the Euclidean norm (L^2 norm). Recall that HD has been deployed in the design of a robust template matching technique in order to detect OD boundaries in [6].

In the absence of ground truth, a viable alternative to validate image segmentation methods is to rely on a variability measure. While the intraobserver variability reflects the reproducibility of a single observer's results, the interobserver variability predicts the differences between the results of multiple observers. The interobserver variability is preferred to the intraobserver one, provided a database is supplied with the results from several observers. Since this is the case with the RIM-ONE database, we resort to the former measure in our experiments. The segmentation performance of an ACM method has been evaluated by computing the HD (as in Definition 1) between the OD contour from the ACM under investigation (white contour in Fig. 7(a)) and the manually delineated OD boundaries (red, green, blue, yellow, and cyan contours in Fig. 7(b)–(f)) of RIM-ONE images by

five domain experts [27]. Collectively, the agreement between each segmented OD region and the gold standard—derived by five experts—is rated with the mean of five HD values thus obtained.

6.4. Discussion

The mean and the standard deviation (SD) of HD between the experts' demarcation and the segmented ODs from the investigated methods were calculated for 169 RIM-ONE images, and the values are recorded in Table 2. Among the experimented algorithms, the Xu-ACM produced an accurate OD segmentation consistently, as evidenced from the least HD value (mean and SD) obtained for every expert's delineated contour. The segmentation results from the Patrick-ACM, Lankton-ACM, and Caselles-ACM are slightly inferior yet comparable to that of the Xu-ACM. The ability of Patrick-ACM to handle ill-defined contours in biomedical images, the local image statistics exploited by the Lankton-ACM to benefit from images

Table 2

Comparison of HD (mean and SD) values measured between the contours demarcated by five experts and the OD boundaries estimated by automated approaches from 169 retinal images in the RIM-ONE database. The overall HD (mean and SD) values are provided in the last column. The minimum HD (mean and SD) values among the outcome of the algorithms are denoted in boldface.

Segmentation method	Mean and SD of HD					Overall HD mean and SD
	Expert 1	Expert 2	Expert 3	Expert 4	Expert 5	
Caselles-ACM	37.65 ± 26.93	37.31 ± 26.27	36.17 ± 14.75	40.95 ± 29.28	44.35 ± 55.67	39.29 ± 20.77
Xu-ACM	30.64 ± 25.41	32.13 ± 25.42	31.39 ± 12.22	34.73 ± 26.57	38.58 ± 53.73	33.49 ± 18.21
Patrick-ACM	35.52 ± 26.30	35.50 ± 26.83	34.42 ± 14.29	38.78 ± 27.71	42.67 ± 53.70	37.38 ± 19.30
Chan-ACM	55.70 ± 37.57	56.66 ± 36.75	55.90 ± 30.52	60.42 ± 41.41	62.93 ± 58.97	58.32 ± 33.59
Shi-ACM	85.64 ± 55.02	87.72 ± 52.80	87.50 ± 48.87	85.54 ± 51.24	89.91 ± 66.65	87.26 ± 51.26
Li2008-ACM	41.92 ± 32.16	46.90 ± 32.66	46.19 ± 25.03	44.32 ± 31.66	48.34 ± 55.48	45.53 ± 26.83
Lankton-ACM	36.08 ± 26.93	35.56 ± 26.17	33.91 ± 14.30	39.64 ± 29.03	43.03 ± 55.62	37.65 ± 20.32
Bernard-ACM	144.30 ± 139.29	145.99 ± 139.91	144.76 ± 138.98	145.26 ± 136.46	143.61 ± 133.01	144.79 ± 135.67
Li2010-ACM	58.70 ± 33.31	60.08 ± 37.49	59.51 ± 31.63	59.78 ± 32.78	62.40 ± 51.66	60.09 ± 29.22
Wu-ACM	66.96 ± 63.14	73.11 ± 65.46	70.85 ± 62.12	67.71 ± 63.33	71.80 ± 74.50	70.09 ± 61.12

Table 3

Outcome of the Wilcoxon signed-rank test—null hypothesis rejection and p value—to determine whether the reduction in the segmentation error due to Xu-ACM is statistically significant compared to nine other ACM techniques. p values less than 0.05 imply that the segmentation errors incurred in Xu-ACM are smaller than the ones from competing approaches with a statistical significance.

Wilcoxon signed-rank test	Competing ACM method with Xu-ACM								
	Caselles-ACM	Patrick-ACM	Chan-ACM	Shi-ACM	Li2008-ACM	Lankton-ACM	Bernard-ACM	Li2010-ACM	Wu-ACM
Hypothesis	1	1	1	1	1	1	1	1	1
p value	2.7853e−14	5.6164e−09	5.7287e−26	6.9637e−29	1.5506e−19	1.4994e−09	1.3355e−28	3.7465e−28	6.1542e−29

Table 4

Mean and SD of the computational time (in seconds) consumed by the ACM techniques listed in Section 6.1. The software system was implemented in MATLAB R2012a on a server of the cluster LILLIGRID composed of 2 hyper-threading 6-core Intel Xeon X5650 processors with 64 GB RAM using Linux OS at the Istituto per le Applicazioni del Calcolo 'Mauro Picone', Italian National Research Council, Naples.

Mean and SD of the computational time in seconds									
Patrick-ACM	Chan-ACM	Xu-ACM	Li2008-ACM	Li2010-ACM	Caselles-ACM	Lankton-ACM	Shi-ACM	Bernard-ACM	Wu-ACM
1.13 ± 0.52	19.66 ± 14.04	7.20 ± 3.86	32.21 ± 10.92	56.45 ± 27.66	10.80 ± 4.08	25.65 ± 8.20	53.55 ± 48.51	269.46 ± 112.96	51.13 ± 41.04

Table 5

Comparison of HD (mean and SD) values from the RIM-ONE retinal images belonging to normal and four glaucoma categories, subsequent to segmentation using the Xu-ACM approach. The last column summarizes the overall HD (mean and SD) values. The minimum HD (mean and SD) values are highlighted in boldface.

Glaucoma condition	Mean and SD of HD					Overall HD mean and SD
	Expert 1	Expert 2	Expert 3	Expert 4	Expert 5	
Normal	29.52 ± 13.44	33.82 ± 28.95	31.90 ± 11.47	35.09 ± 19.08	35.98 ± 35.60	33.26 ± 14.39
Early	25.06 ± 8.76	22.80 ± 8.33	27.59 ± 9.41	26.68 ± 12.02	27.52 ± 12.08	25.93 ± 8.19
Moderate	35.05 ± 19.09	35.85 ± 19.75	36.75 ± 18.99	40.48 ± 18.79	59.65 ± 79.11	41.56 ± 25.20
Deep	47.05 ± 75.99	27.69 ± 10.91	27.29 ± 12.45	41.77 ± 70.67	59.72 ± 134.61	40.70 ± 37.50
OHT	22.25 ± 11.47	25.09 ± 8.36	28.39 ± 10.40	23.41 ± 12.43	24.70 ± 11.55	24.77 ± 10.12

with heterogeneous feature profiles, and the improvement offered by Caselles-ACM in the detection of boundaries with gradients that largely differ have indeed paid off while segmenting the OD from the retinal images. Despite the claim concerning the computational advantage of Shi-ACM, in practice we fail to observe this from the execution time listed in Table 4; moreover, it did not fare better than most of the ACMs, for instance, Patrick-ACM, in the context of the OD segmentation accuracy. Reportedly, the Chan-ACM is capable of segmenting difficult images, and the Li2008-ACM can deal with intensity inhomogeneities and weak boundaries; nevertheless, these techniques led to unsatisfactory OD segmentation. Apparently, the efforts of Li2010-ACM to ensure regularity during the level set evolution and the intrinsic smoothing of the Bernard-ACM to tackle the additive noise turn out to be counterproductive as corroborated by the large HD values. It is noteworthy that the performance of Wu-ACM is disappointingly poor, even though it aims to rectify the inherent limitations of Xu-ACM. The overall accuracy of an ACM-based automated OD segmentation is indicated by the mean (and the SD) of HD computed with the boundaries drawn by experts; interestingly, the values mentioned in the last column of Table 2 remain in favor of the Xu-ACM approach.

To validate whether the relative decrease of segmentation error incurred in Xu-ACM with regard to nine other ACM methods is statistically significant, we have conducted the *Wilcoxon signed-rank test* by comparing the HD values from a competing method and Xu-ACM for 169 retinal images. The Wilcoxon signed-rank test is a nonparametric statistical hypothesis test to assess if the population mean rank of two related samples differ. Unlike the *paired Student's t-test*, the population need not be assumed to be normally distributed, which is the motivation behind the choice of this test. The p values and the outcome of the hypothesis test—"1" implying a statistical difference and "0" negating such a difference—are recorded in Table 3. The p values less than 0.05 are considered to be statistically significant, thereby providing a supportive evidence for the improved performance of Xu-ACM in all the comparisons.

To understand the impact of various stages of glaucoma on the detection accuracy of OD contours by the Xu-ACM, the HD (mean and SD) values are grouped in Table 5 for the following retinal image categories: (i) normal; (ii) early glaucoma; (iii) moderate glaucoma; (iv) deep glaucoma; and (v) OHT. The HD values computed for the OD contours are satisfactory for the images classified as early and deep glaucoma. Nevertheless, owing to the presence of PPA that interferes with the segmentation process, the contour detection accuracy is most adversely affected in the moderate glaucoma images. On the contrary, the Xu-ACM could manage to segment the OD contours in the OHT images with an impressive accuracy, and hence the proposed technique is envisaged to have application in an automated system for detection of the OHT condition and early glaucoma.

Among the RIM-ONE database images, the Xu-ACM offered outstanding OD segmentation results in 94% of the cases. A few troublesome retinal images, with which the Xu-ACM encountered difficulties and yielded substandard results, are displayed in Fig. 8; overexposure during photographing and the presence of PPA are accounted for the inferior performance of a contour detection algorithm.

Furthermore, the segmented ODs from the Xu-ACM were subjectively assessed by two independent ophthalmological experts,⁴ who graded the segmentation quality under four headings: (i) excellent; (ii) good; (iii) average; and (iv) poor. It is noteworthy to state that out of 169 retinal images, 135 and 120 segmented OD images were classified to be either excellent or good by ophthalmologist 1 and 2, respectively. For a concise report on the qualitative assessment by the ophthalmologists, one may refer to Table 6.

⁴ Third and fourth authors of this article.

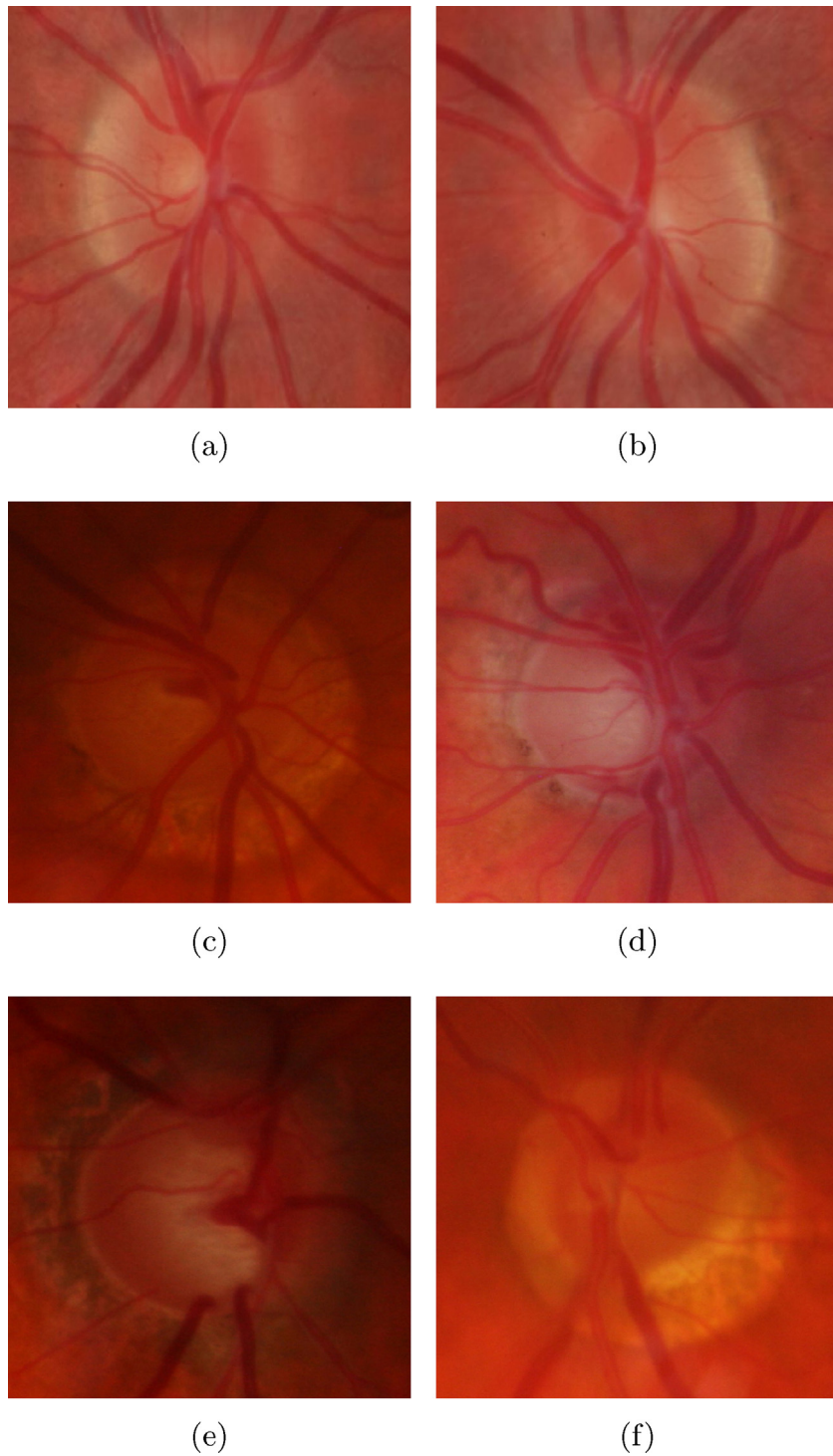


Fig. 8. Notorious retinal fundus images posing challenges to the Xu-ACM algorithm while segmenting the OD either due to the presence of PPA or due to overexposure: (a) normal with PPA; (b) overexposed and normal; (c) moderate glaucoma with PPA; (d) overexposed and moderate glaucoma; (e) deep glaucoma with PPA; (f) OHT with PPA.

Table 6
Level of agreement between the OD contours estimated independently by two ophthalmologists and the OD boundaries segmented by the Xu-ACM approach.

Ophthalmologist	Subjective grading			
	Excellent	Good	Average	Poor
1	57	78	26	8
2	61	59	39	10

7. Conclusion

This article concerns a systematic performance comparison of a judicious choice of ten widely recommended ACM techniques, which are employed to segment the OD from 169 annotated retinal fundus images of various categories. The outcome of the study suggests that the GVF-based Xu-ACM initialized with the contour produced by the CHT outclasses the rest of the state-of-the-art variants of ACM—Caselles-ACM, Patrick-ACM, Chan-ACM, Shi-ACM,

Li2008-ACM, Lankton-ACM, Bernard-ACM, Li2010-ACM, and Wu-ACM—in segmenting the OD contours from a wide collection of retinal images. Furthermore, it is encouraging to note that the computational overhead associated with the Xu-ACM implementation is the second least as portrayed in Table 4. We envisage that the Xu-ACM could possibly be applied for measuring the *vertical cup-to-disc ratio* on retinal fundus images, thus facilitating automatic detection of early glaucoma and OHT condition. The future direction of research would be to tackle the interference of PPA located adjacent to the OD with the segmentation process, thereby further improving the accuracy of a segmentation scheme.

References

- [1] L. Gagnon, M. Lalonde, M. Beaulieu, M.-C. Boucher, Procedure to detect anatomical structures in optical fundus images, in: Proceedings of the SPIE: Medical Imaging, vol. 4322, San Diego, CA, 2001, pp. 1218–1225.
- [2] S. Kingman, Glaucoma is second leading cause of blindness globally, Bull. World Health Organ. 82 (11) (2004) 887–888.
- [3] J. Nayak, U.R. Acharya, P.S. Bhat, N. Shetty, T.-L. Lim, Automated diagnosis of glaucoma using digital fundus images, J. Med. Syst. 33 (5) (2009) 337–346.
- [4] C.A. Johnson, The decision tree in glaucoma diagnosis, Rev. Optom. 1 (2) (2009) 146.
- [5] M.S. Haleem, L. Han, J.V. Hemert, B. Li, Automatic extraction of retinal features from colour retinal images for glaucoma diagnosis: a review, Comput. Med. Imaging Graph. 37 (7) (2013) 581–596.
- [6] M. Lalonde, M. Beaulieu, L. Gagnon, Fast and robust optic disc detection using pyramidal decomposition and Hausdorff-based template matching, IEEE Trans. Med. Imaging 20 (11) (2001) 1193–1200.
- [7] H. Li, O. Chutatape, Automated feature extraction in color retinal images by a model based approach, IEEE Trans. Biomed. Eng. 51 (2) (2004) 246–254.
- [8] M. Foracchia, E. Grisan, A. Ruggeri, Detection of optic disc in retinal images by means of a geometrical model of vessel structure, IEEE Trans. Med. Imaging 23 (10) (2004) 1189–1195.
- [9] M. Niemeijer, M.D. Abràmoff, B.V. Ginneken, Segmentation of the optic disc, macula and vascular arch in fundus photographs, IEEE Trans. Med. Imaging 26 (1) (2007) 116–127.
- [10] A.A.-H.A.-R. Youssif, A.Z. Ghalwash, A.S.A.-R. Ghoneim, Optic disc detection from normalized digital fundus images by means of a vessels' direction matched filter, IEEE Trans. Med. Imaging 27 (1) (2008) 11–18.
- [11] S. Lu, J.H. Lim, Automatic optic disc detection from retinal images by a line operator, IEEE Trans. Biomed. Eng. 58 (1) (2011) 88–94.
- [12] S. Lu, Accurate and efficient optic disc detection and segmentation by a circular transformation, IEEE Trans. Med. Imaging 30 (12) (2011) 2126–2133.
- [13] V. Caselles, R. Kimmel, G. Sapiro, Geodesic active contours, Int. J. Comput. Vis. 22 (1) (1997) 61–79.
- [14] C. Xu, J.L. Prince, Snakes, shapes, and gradient vector flow, IEEE Trans. Image Process. 7 (3) (1998) 359–369.
- [15] C. Xu, D.L. Pham, J.L. Prince, Image segmentation using deformable models, in: J.M. Fitzpatrick, M. Sonka (Eds.), Handbook of Medical Imaging, vol. 2, SPIE, Washington, 2000, pp. 129–174.
- [16] A. Tsai, A. Yezzi Jr., W. Wells, C. Tempany, D. Tucker, A. Fan, W.E. Grimson, A. Willsky, A shape-based approach to the segmentation of medical imagery using level sets, IEEE Trans. Med. Imaging 22 (2) (2003) 137–154.
- [17] J. Lowell, A. Hunter, D. Steel, A. Basu, R. Ryder, E. Fletcher, L. Kennedy, Optic nerve head segmentation, IEEE Trans. Med. Imaging 23 (2) (2004) 256–264.
- [18] R. Chrástek, M. Wolf, K. Donath, H. Niemann, D. Paulus, T. Hothorn, B. Lausen, R. Lämmer, C.Y. Mardin, G. Michelson, Automated segmentation of the optic nerve head for diagnosis of glaucoma, Med. Image Anal. 9 (4) (2005) 297–314.
- [19] L.D. Cohen, I. Cohen, Finite-element methods for active contour models and balloons for 2-D and 3-D images, IEEE Trans. Pattern Anal. Mach. Intell. 15 (11) (1993) 1131–1147.
- [20] D. Kucera, Segmentation of Multidimensional Image Data in Medicine, TU, Brno, 1996 (Ph.D. thesis).
- [21] J. Xu, O. Chutatape, E. Sung, C. Zheng, P.C.T. Kuan, Optic disk feature extraction via modified deformable model technique for glaucoma analysis, Pattern Recognit. 40 (7) (2007) 2063–2076.
- [22] M. Kass, A. Witkin, D. Terzopoulos, Snakes: active contour models, Int. J. Comput. Vis. 1 (4) (1988) 321–331.
- [23] T.F. Chan, L.A. Vese, Active contours without edges, IEEE Trans. Image Process. 10 (2) (2001) 266–277.
- [24] G.D. Joshi, J. Sivaswamy, S.R. Krishnadas, Optic disk and cup segmentation from monocular color retinal images for glaucoma assessment, IEEE Trans. Med. Imaging 30 (6) (2011) 1192–1205.
- [25] H. Yu, E.S. Barriga, C. Agurto, S. Echegaray, M.S. Pattichis, W. Bauman, P. Soliz, Fast localization and segmentation of optic disk in retinal images using directional matched filtering and level sets, IEEE Trans. Inf. Technol. Biomed. 16 (4) (2012) 644–657.
- [26] Y. Zhang, B.J. Matuszewski, L. Shark, C.J. Moore, Medical image segmentation using new hybrid level-set method, in: Proceedings of the Fifth International Conference BioMedical Visualization: Information Visualization in Medical and Biomedical Informatics (MediVis 2008), London, UK, 2008, pp. 71–76.
- [27] F. Fumero, S. Alayón, J.L. Sanchez, J. Sigut, M. Gonzalez-Hernandez, Rim-one: an open retinal image database for optic nerve evaluation, in: Proceedings of the 24th International Symposium on Computer-Based Medical Systems (CBMS), Bristol, UK, 2011, pp. 1–6.
- [28] A. Aquino, M.E. Gegúndez-Arias, D. Marín, Detecting the optic disc boundary in digital fundus images using morphological, edge detection, and feature extraction techniques, IEEE Trans. Med. Imaging 29 (11) (2010) 1860–1869.
- [29] P. Treigys, V. Šaltenis, G. Dzemyda, V. Barzdžiukas, A. Paunksnis, Automated optic nerve disc parameterization, Informatica 19 (3) (2008) 403–420.
- [30] N. Otsu, A threshold selection method from gray level histograms, IEEE Trans. Syst. Man Cybern. 9 (1) (1979) 62–66.
- [31] P. Brigger, J. Hoeg, M. Unser, B-spline snakes: a flexible tool for parametric contour detection, IEEE Trans. Image Process. 9 (9) (2000) 1484–1496.
- [32] Y. Shi, W.C. Karl, A real-time algorithm for the approximation of level-set-based curve evolution, IEEE Trans. Image Process. 17 (5) (2008) 645–656.
- [33] C. Li, C.-Y. Kao, J.C. Gore, Z. Ding, Minimization of region-scalable fitting energy for image segmentation, IEEE Trans. Image Process. 17 (10) (2008) 1940–1949.
- [34] S. Lankton, A. Tannenbaum, Localizing region-based active contours, IEEE Trans. Image Process. 17 (11) (2008) 2029–2039.
- [35] O. Bernard, D. Friboulet, P. Thévenaz, M. Unser, Variational B-spline level-set: a linear filtering approach for fast deformable model evolution, IEEE Trans. Image Process. 18 (6) (2009) 1179–1191.
- [36] C. Li, C. Xu, C. Gui, M.D. Fox, Distance regularized level set evolution and its application to image segmentation, IEEE Trans. Image Process. 19 (12) (2010) 3243–3254.
- [37] Y. Wu, Y. Wang, Y. Jia, Adaptive diffusion flow active contours for image segmentation, Comput. Vis. Image Underst. 117 (6) (2013) 1421–1435.
- [38] N.P. Tiilikainen, A comparative study of active contour snakes, graduate level project report, Copenhagen University, Denmark, 2007.
- [39] D.P. Huttenlocher, G.A. Klanderman, W.J. Rucklidge, Comparing images using the Hausdorff distance, IEEE Trans. Pattern Anal. Mach. Intell. 15 (9) (1993) 850–863.